Above-threshold-ionization spectra from the core region of a time-dependent wave packet: An *ab initio* time-dependent approach

Dmitry A. Telnov[1,*] and Shih-I Chu (朱時宜)[2,3,†]

[1]*Department of Physics, St. Petersburg State University, 198504 St. Petersburg, Russia*

[2]*Department of Chemistry, University of Kansas, Lawrence, Kansas 66045, USA*

[3]*Center for Quantum Science and Engineering, and Department of Physics, National Taiwan University, Taipei 106, Taiwan*

(Received 3 October 2008; revised manuscript received 11 January 2009; published 27 April 2009)

We present a method for accurate and efficient treatment of the time-dependent Schrödinger equation and electron energy and angular distributions after above-threshold multiphoton ionization. The procedure does not require propagation of the wave packet at large distances, making use of the wave function in the core region. It is based on the extension of the Kramers-Henneberger picture of the ionization process while the final expressions involve the wave function in the laboratory frame only. The approach is illustrated by a case study of above-threshold ionization of the hydrogen atom subject to intense laser pulses. The ejected electron energy and angle distributions have been calculated and analyzed. We explore the electron spectrum dependence on the duration of the laser pulse and carrier-envelope phase.

DOI: 10.1103/PhysRevA.79.043421 PACS number(s): 32.80.Rm, 32.80.Qk

I. INTRODUCTION

Recently the phenomenon of above-threshold ionization (ATI) and investigations of resulting electron distributions attracted much new interest. This is related to advances in laser technology which made possible generation of short and intense laser pulses [1]. For such pulses the absolute or carrier-envelope phase (CEP) plays an important role [2], and properties of the ejected electrons momentum (or energy-angle) distributions differ significantly from those for long pulses. Recent experiments [3,4] were able to measure high-resolution fully differential data on ATI of noble gases. Thus accurate theoretical description of the electron distributions becomes an important and timely task. Traditionally many theoretical ATI studies are based on the strong-field approximation (SFA) [5]; this approach has its origin in earlier works of Keldysh, Faisal, and Reiss [6] as well as in the semiclassical rescattering model [7]. While SFA-based models result in rather simple theoretical expressions and produce electron spectra that qualitatively resemble those obtained with accurate numerical wave functions, they fail to give quantitative agreement with more accurate theories. The discrepancy can be as large as several orders of magnitude [8]. Recent calculations of two-dimensional (2D) electron momentum distributions by both SFA and solution of the time-dependent Schrödinger equation (TDSE) [9] show that SFA cannot reproduce some features of the distributions even qualitatively. An alternative to SFA can be a numerical solution of TDSE and making use of accurate time-dependent wave functions. Certainly, this approach is much more demanding computationally but it can provide results good enough for correct description of the electron spectra including subtle effects related to CEP dependence.

Normally one needs accurate wave functions in a large space domain to obtain correct distributions of the ejected electrons. This is because unbound parts of the wave packet spread out of the core region, and conventional expressions for the transition amplitude which come from the scattering theory [10] utilize these parts of the wave function. Solving TDSE within all required space volume can be a very difficult computational problem. To circumvent the problem, in Ref. [11] the whole space was partitioned in two regions. In the inner region, the wave function was obtained by solving exact TDSE numerically. In the outer region the Coulomb interaction was neglected, and the wave function was propagated analytically in the laser field only. For large enough inner region, the final results did not depend on the position of the boundary between the two regions. In the present paper, we propose another approach. It is based on alternative expression for the transition amplitude which utilizes the core part of the wave function. In this approach, all necessary information regarding the outgoing electron distributions can be extracted from the vicinity of the atomic core, so no wave-function computations at large distances are required.

The paper is organized as follows. In Sec. II, we derive the desired expression for the transition amplitude in the general case and also provide some specific formulas for the Coulomb interaction with the atomic core. In Sec. III, we present results of ATI calculations of the hydrogen atom subject to an intense laser pulse. Section IV contains concluding remarks.

II. THEORY OF ELECTRON SPECTRA

A. General formulation

We start from the time-dependent Schrödinger equation for the electron wave function,

$$i\frac{\partial}{\partial t}\Psi(\boldsymbol{r},t)=[H_0+V(\boldsymbol{r},t)]\Psi(\boldsymbol{r},t). \tag{1}$$

Here the term $V(\boldsymbol{r},t)$ describes the interaction with the laser pulse and H_0 is the unperturbed Hamiltonian,

*telnov@pcqnt1.phys.spbu.ru

†sichu@ku.edu

$$H_0 = -\frac{1}{2}\nabla^2 + U(\boldsymbol{r}), \tag{2}$$

$U(\boldsymbol{r})$ being the atomic core potential. We assume that the pulse begins at $t=0$ and ends at $t=t_\mathrm{f}$, therefore the interaction $V(\boldsymbol{r},t)$ vanishes for any time moment outside interval $[0,t_\mathrm{f}]$. Before the pulse, the electron wave function $\Psi_\mathrm{i}(\boldsymbol{r},t)$ describes one of the bound states of the core potential $U(\boldsymbol{r})$,

$$\Psi_\mathrm{i}(\boldsymbol{r},t) = \psi_\mathrm{i}(\boldsymbol{r})\exp(-iE_\mathrm{i}t), \tag{3}$$

with E_i being the energy of the initial state. The laser field causes transitions to other bound and unbound states, and after the pulse the electron quantum state represents a wave packet which contains bound (discrete spectrum) as well as unbound (continuous spectrum) contributions. The transition amplitude to any eigenstate of the unperturbed Hamiltonian with the energy E_f (the final state),

$$\Psi_\mathrm{f}(\boldsymbol{r},t) = \psi_\mathrm{f}(\boldsymbol{r})\exp(-iE_\mathrm{f}t), \tag{4}$$

can be calculated as a projection of the wave packet $\Psi(\boldsymbol{r},t)$ onto the final state at $t=t_\mathrm{f}$ (or any time $t>t_\mathrm{f}$),

$$T_\mathrm{fi} = \langle \Psi_\mathrm{f}(\boldsymbol{r},t_\mathrm{f})|\Psi(\boldsymbol{r},t_\mathrm{f})\rangle. \tag{5}$$

Expression (5) is simple and can be used in practical calculations once the wave packet $\Psi(\boldsymbol{r},t)$ is constructed [for example, by solving Eq. (1)]. However, there is some technical problem when applying Eq. (5) for evaluation of transition amplitudes to unbound states, that is ionization amplitudes. In this case, the result is nonzero due to the unbound part of the wave packet which is spreading out of the core region. After the pulse, this part of the wave packet can be found far from the core, and using Eq. (5) requires accurate representation of the wave function at large distances. For example, for the electron momentum 1 a.u., laser wavelength 800 nm, and pulse duration 10 optical cycles (approximately 27 fs), the important distances from the core can be as large as 1000 a.u. Construction of an accurate time-dependent wave function in the volume with linear dimensions of 1000 a.u. can be a demanding computational task. Using remote space regions may have its advantages, however. Thus, one can apply asymptotic forms of the final states $\Psi_\mathrm{f}(\boldsymbol{r},t)$ instead of the exact wave functions. This is particularly important for calculations of double ionization in two-electron systems where fully correlated two-electron final states cannot be easily obtained [12].

Our goal, however, is to avoid propagation of the wave function at very large distances. That is why we need to consider alternative expressions for the transition amplitude. Another commonly used expression can be obtained from the integral equation which follows immediately from Eq. (1),

$$\Psi(\boldsymbol{r},t) = \Psi_\mathrm{i}(\boldsymbol{r},t) - i\int_0^t dt'\ \exp[-i(t-t')H_0]V(\boldsymbol{r},t')\Psi(\boldsymbol{r},t'). \tag{6}$$

Making a projection of the wave function $\Psi(\boldsymbol{r},t)$ onto a final state $\Psi_\mathrm{f}(\boldsymbol{r},t)$ at time t_f results in the following expression for the amplitude T_fi:

$$T_\mathrm{fi} = \delta_\mathrm{fi} - i\int_0^{t_\mathrm{f}} dt\langle \Psi_\mathrm{f}(\boldsymbol{r},t)|V(\boldsymbol{r},t)|\Psi(\boldsymbol{r},t)\rangle$$

$$= \delta_\mathrm{fi} - i\int_0^{t_\mathrm{f}} dt\ \exp(iE_\mathrm{f}t)\langle \psi_\mathrm{f}(\boldsymbol{r})|V(\boldsymbol{r},t)|\Psi(\boldsymbol{r},t)\rangle. \tag{7}$$

Here the Kronecker symbol δ_fi accounts for the possible situation when the final state coincides with the initial state. Equation (7), however, is not very helpful for us either. It contains a matrix element of the interaction operator $V(\boldsymbol{r},t)$. Within the commonly used (and well justified for optical range of radiation wavelengths) dipole approximation, this operator is a multiplication by the electron coordinate (in the length gauge). Thus the spatial integration in Eq. (7) emphasizes large distances, just like Eq. (5) does. In the velocity gauge $V(\boldsymbol{r},t)$ is a differential operator but this does not improve the situation.

To derive a suitable expression for the transition amplitude T_fi, we return to Eq. (1) and adopt the dipole approximation. Instead of vector potential or electric field strength, we make use of the time-dependent quantity $\boldsymbol{b}(t)$ which has the meaning of the displacement of the "classical" electron (a particle with the mass equal to unity and the charge equal to minus unity) under the influence of the laser field only. Then Eq. (1) will take the form,

$$i\frac{\partial}{\partial t}\Psi^\mathrm{L}(\boldsymbol{r},t) = \left[-\frac{1}{2}\nabla^2 - (\ddot{\boldsymbol{b}}\cdot\boldsymbol{r}) + U(\boldsymbol{r})\right]\Psi^\mathrm{L}(\boldsymbol{r},t), \tag{8}$$

for the interaction in the length gauge, and the form,

$$i\frac{\partial}{\partial t}\Psi^\mathrm{V}(\boldsymbol{r},t) = \left[\frac{1}{2}(-i\nabla + \dot{\boldsymbol{b}})^2 + U(\boldsymbol{r})\right]\Psi^\mathrm{V}(\boldsymbol{r},t), \tag{9}$$

for the interaction in the velocity gauge. One and two dots above $\boldsymbol{b}$ denote the first and the second derivative with respect to time. The wave functions $\Psi^\mathrm{L}(\boldsymbol{r},t)$ and $\Psi^\mathrm{V}(\boldsymbol{r},t)$ are related to each other by a simple gauge transformation,

$$\Psi^\mathrm{V}(\boldsymbol{r},t) = \Psi^\mathrm{L}(\boldsymbol{r},t)\exp[-i(\dot{\boldsymbol{b}}\cdot\boldsymbol{r})]. \tag{10}$$

Now we make a transition to the Kramers-Henneberger (KH) [13,14] frame of reference with the help of the following transformation:

$$\Psi^\mathrm{V}(\boldsymbol{r},t) = \Psi^\mathrm{K}(\boldsymbol{R},t)\exp\left(-\frac{i}{2}\int_0^t \dot{\boldsymbol{b}}^2 d\tau\right), \tag{11}$$

$$\boldsymbol{R} = \boldsymbol{r} - \boldsymbol{b}(t). \tag{12}$$

The wave function $\Psi^\mathrm{K}(\boldsymbol{R},t)$ satisfies the time-dependent Schrödinger equation without external field but with the atomic core moving according to the classical law $\boldsymbol{b}(t)$,

$$i\frac{\partial}{\partial t}\Psi^\mathrm{K}(\boldsymbol{R},t) = \left[-\frac{1}{2}\nabla^2 + U(\boldsymbol{R}+\boldsymbol{b})\right]\Psi^\mathrm{K}(\boldsymbol{R},t). \tag{13}$$

Before the pulse, $\boldsymbol{b}(t\le 0)=0$, and the KH frame coincides with the original laboratory frame. We can split the Hamiltonian in the right-hand side of Eq. (13) in two parts, "unperturbed" Hamiltonian H_0 and interaction operator $V(\boldsymbol{R},t)$,

$$H_0 = -\frac{1}{2}\nabla^2 + U(\boldsymbol{R}), \tag{14}$$

$$V(\boldsymbol{R},t) = U(\boldsymbol{R}+\boldsymbol{b}) - U(\boldsymbol{R}). \tag{15}$$

Note that H_0 is exactly the same as it was defined in the laboratory frame by Eq. (2), and $V(\boldsymbol{R},t)$ is decreasing as $1/R^2$ at large R (the Coulomb interaction with the atomic core at large distances is assumed). After the pulse, the resulting displacement $\boldsymbol{b}(t_f)$ is not necessarily equal to zero, in contrast with the resulting momentum $\dot{\boldsymbol{b}}(t_f)$ which must vanish for any real laser pulse (the zero-net-force condition, see, e.g., Ref. [15]). In the following, however, we will restrict to the case of the laser pulses which satisfy the both zero-net-force and zero-net-displacement conditions. In this case, the interaction [Eq. (15)] vanishes at large distances in the space domain as well as before and after the pulse in the time domain. Since the time-dependent problem in the KH frame differs from that in the laboratory frame by the specific form of the interaction term $V(\boldsymbol{R},t)$ only, one can proceed with the integral Eq. (6) and write down the transition amplitude in the form [Eq. (7)],

$$T_{\mathrm{fi}} = \delta_{\mathrm{fi}} - i\int_0^{t_f} dt \langle \Psi_f(\boldsymbol{R},t)|U(\boldsymbol{R}+\boldsymbol{b}) - U(\boldsymbol{R})|\Psi^K(\boldsymbol{R},t)\rangle. \tag{16}$$

Although Eq. (16) is derived in the *KH frame*, it also gives the transition amplitude in the *laboratory frame* provided the zero-net-displacement condition is satisfied, and both frames coincide at the end of the pulse. With the help of Eqs. (4), (11), and (10), one can express T_{fi} through the wave functions defined in the laboratory frame, using the velocity or length gauge,

$$T_{\mathrm{fi}} = \delta_{\mathrm{fi}} - i\int_0^{t_f} dt \exp\left(iE_f t + \frac{i}{2}\int_0^t \dot{\boldsymbol{b}}^2 d\tau\right) \times \langle \psi_f(\boldsymbol{r}-\boldsymbol{b})|U(\boldsymbol{r}) - U(\boldsymbol{r}-\boldsymbol{b})|\Psi^V(\boldsymbol{r},t)\rangle, \tag{17}$$

$$T_{\mathrm{fi}} = \delta_{\mathrm{fi}} - i\int_0^{t_f} dt \exp\left(iE_f t + \frac{i}{2}\int_0^t \dot{\boldsymbol{b}}^2 d\tau\right) \times \langle \psi_f(\boldsymbol{r}-\boldsymbol{b})|U(\boldsymbol{r}) - U(\boldsymbol{r}-\boldsymbol{b})|\exp[-i(\dot{\boldsymbol{b}}\cdot\boldsymbol{r})]\Psi^L(\boldsymbol{r},t)\rangle. \tag{18}$$

The interaction term $U(\boldsymbol{r})-U(\boldsymbol{r}-\boldsymbol{b})$ decreases at least as $1/r^2$ at large r, therefore the spatial integration in Eqs. (17) and (18) emphasizes the core region of the wave packet.

We note that the KH frame has been widely used to solve TDSE when treating stabilization of atoms in superintense laser fields (see the review paper [16] and references therein). In Ref. [17], simulations of the wave packet in the KH frame have been made for the analysis of stabilization and calculations of the ATI spectra of the hydrogen atom. In our current approach, the procedure is different. We employ the KH frame to derive the expressions for the transition amplitude only. Our final Eqs. (17) and (18) do not contain quantities which must be calculated in the KH frame. The wave packets $\Psi^V(\boldsymbol{r},t)$ and $\Psi^L(\boldsymbol{r},t)$ are obtained by solving TDSE in the *laboratory frame*.

If unbound final states are used in Eqs. (17) or (18), then T_{fi} provides the ionization amplitude. Any energy eigenvalue E_f in the continuum corresponds to infinite number of eigenstates, and one has to select some specific eigenstates as the final states to obtain the amplitudes T_{fi} with particular physical meaning. As discussed in the scattering theory (see, e.g., Ref. [10]), to obtain angular (or momentum) distributions of the ejected electrons, the final states $\psi_{\boldsymbol{k}}^-(\boldsymbol{r})$ should be used which have plane waves and incoming spherical waves in asymptotic forms at large distances. The states $\psi_{\boldsymbol{k}}^-(\boldsymbol{r})$ corresponding to different momenta $\boldsymbol{k}$ and $\boldsymbol{k}'$ are orthogonal to each other, and we adopt the following orthogonality and normalization condition:

$$\langle \psi_{\boldsymbol{k}'}^-(\boldsymbol{r})|\psi_{\boldsymbol{k}}^-(\boldsymbol{r})\rangle = \delta^{(3)}(\boldsymbol{k}-\boldsymbol{k}'). \tag{19}$$

Then the differential ionization probability corresponding to ejection of the electron with the energy E_f within the unit energy interval and unit solid angle can be expressed as follows:

$$\frac{\partial^2 P}{\partial E_f\, \partial\, \Omega} = \sqrt{2E_f}|T_{\mathrm{fi}}|^2. \tag{20}$$

B. Specific expressions for the Coulomb interaction with the core

If interaction with the core is represented by the Coulomb potential,

$$U(\boldsymbol{r}) = -\frac{Z_c}{r}, \tag{21}$$

Z_c being the core charge ($Z_c=1$ for the hydrogen atom), then the general expressions of Sec. II A can be further elaborated. First, the final unbound states $\psi_{\boldsymbol{k}}^-(\boldsymbol{r})$ in the Coulomb field are known in a rather simple closed form,

$$\psi_{\boldsymbol{k}}^-(\boldsymbol{r}) = \frac{1}{2\pi}\sqrt{\frac{\nu}{\exp(2\pi\nu)-1}}\exp[i(\boldsymbol{k}\cdot\boldsymbol{r})] \times M(i\nu,1,-i[kr+(\boldsymbol{k}\cdot\boldsymbol{r})]), \tag{22}$$

where $M(a,c,x)$ is the confluent hypergeometric function [18] and ν is the Coulomb parameter,

$$\nu = -\frac{Z_c}{k}. \tag{23}$$

Second, one can simplify the spatial integration in Eqs. (17) and (18) accurately accounting for the Coulomb singularities of the integrand. The space integrals in Eqs. (17) and (18) are two-center integrals which can be recast in the following form:

$$\langle \psi(\boldsymbol{r}-\boldsymbol{b}/2)|U(\boldsymbol{r}+\boldsymbol{b}/2) - U(\boldsymbol{r}-\boldsymbol{b}/2)|\phi(\boldsymbol{r}+\boldsymbol{b}/2)\rangle, \tag{24}$$

with the appropriate functions $\psi(\boldsymbol{r})$ and $\phi(\boldsymbol{r})$. Introducing the prolate spheroidal coordinates ξ and η with the half-separation between the centers $a=\frac{1}{2}b$,

$$r\cos\vartheta = a\xi\eta, \quad r\sin\vartheta = a\sqrt{(\xi^2-1)(1-\eta^2)}, \tag{25}$$

(r and ϑ are the spherical polar coordinates), one can express the difference of the Coulomb core potentials as follows:

$$U\left(\boldsymbol{r}+\frac{\boldsymbol{b}}{2}\right) - U\left(\boldsymbol{r}-\frac{\boldsymbol{b}}{2}\right) = \frac{Z_c}{a^2}\frac{b\eta}{\xi^2-\eta^2}. \tag{26}$$

Then the two-center integral Eq. (24) takes the form without the Coulomb singularities,

$$\langle\psi(\boldsymbol{r}-\boldsymbol{b}/2)|U(\boldsymbol{r}+\boldsymbol{b}/2)-U(\boldsymbol{r}-\boldsymbol{b}/2)|\phi(\boldsymbol{r}+\boldsymbol{b}/2)\rangle = abZ_c\int_0^{2\pi}d\varphi\int_1^{\infty}d\xi\int_{-1}^{1}d\eta\eta\psi^*(\boldsymbol{r}-\boldsymbol{b}/2)\phi(\boldsymbol{r}+\boldsymbol{b}/2). \tag{27}$$

With the help of Eq. (27), one can calculate the two-center spatial integrals in the ionization amplitudes Eqs. (17) and (18). For example, with the length gauge wave function used, the differential ionization probability can be expressed as follows:

$$\frac{\partial^2 P}{\partial E_f\,\partial\Omega} = \sqrt{2E_f}Z_c^2\left|\int_0^{t_f}dtb(t)\exp\left[iE_f t+\frac{i}{2}\int_0^t\dot{\boldsymbol{b}}^2d\tau - \frac{i}{2}(\dot{\boldsymbol{b}}\cdot\boldsymbol{b})\right]\int_0^{2\pi}d\varphi\int_a^{\infty}d(a\xi)\int_{-1}^{1}d\eta\eta \times[\psi_{\boldsymbol{k}}^-(\boldsymbol{r}-\boldsymbol{b}/2)]^*\exp[-i(\dot{\boldsymbol{b}}\cdot\boldsymbol{r})]\Psi^L(\boldsymbol{r}+\boldsymbol{b}/2,t)\right|^2. \tag{28}$$

III. ATI OF ATOMIC HYDROGEN

As a case study, we consider above-threshold ionization of the hydrogen atom by long and short laser pulses. We choose a sine-squared pulse envelope in the vector potential form. In our notations, the classical velocity $\dot{\boldsymbol{b}}(t)$ has the following expression:

$$\dot{\boldsymbol{b}} = \frac{\boldsymbol{F}_0}{\omega}\sin^2\left(\frac{\omega t}{2N}\right)\sin(\omega t+\alpha). \tag{29}$$

Then the classical acceleration and displacement appear as follows:

$$\ddot{\boldsymbol{b}} = \boldsymbol{F}_0\left[\sin^2\left(\frac{\omega t}{2N}\right)\cos(\omega t+\alpha)+\frac{1}{2N}\sin\left(\frac{\omega t}{N}\right)\sin(\omega t+\alpha)\right], \tag{30}$$

$$\boldsymbol{b} = -\frac{\boldsymbol{F}_0}{2\omega^2}\left[\cos(\omega t+\alpha)-\frac{N}{2(N+1)}\cos\left(\frac{N+1}{N}\omega t+\alpha\right) - \frac{N}{2(N-1)}\cos\left(\frac{N-1}{N}\omega t+\alpha\right)+\frac{1}{N^2-1}\cos\alpha\right]. \tag{31}$$

In Eqs. (29)–(31), ω is the carrier frequency, $\boldsymbol{F}_0$ has the meaning of the peak electric field strength (more precisely, F_0/ω is the peak value for the pulse envelope in the vector potential form), N denotes the number of optical cycles in the pulse, and α is the carrier-envelope phase. The linear polarization of the laser field is assumed.

We solve the time-dependent Schrödinger Eq. (8) with the interaction term in the length gauge; the atomic core potential is $U(\boldsymbol{r})=-1/r$. The ground state of the hydrogen atom is selected as the initial state, and then the wave function is propagated in time using the split-operator technique and generalized pseudospectral (GPS) discretization of the spherical polar coordinates; the details of the method were discussed elsewhere [19,20]. The radial coordinate is restricted to the domain from 0 to 60 a.u.; between 40 and 60 a.u. we apply an absorber which smoothly brings down the wave function without spurious reflections. Absorbed parts of the wave packet localized beyond 40 a.u. describe unbound states populated during the ionization process. Because of the absorber, the normalization integral of the wave function decreases in time. Calculated after the pulse, it gives the survival probability P_s,

$$P_s = \int d^3r|\Psi^L(\boldsymbol{r},t_f)|^2. \tag{32}$$

Then the ionization probability appears as

$$P_i = 1-P_s. \tag{33}$$

Finite range of the radial coordinate (yet large enough to contain all physically important space domain) allows to maintain high accuracy while using moderate number of grid points (we use 64 points for discretization of the radial coordinate and 24 points for discretization of the angular coordinate). Since the wave function is not computed at very large distances, making use of Eqs. (5) or (7) to calculate the electron distributions is inappropriate and leads to erroneous results. On the contrary, Eq. (28), as our computations show, provides accurate electron distributions.

In Eq. (28), we integrate in the time domain with the help of the fast Fourier transform (FFT) routines, and the space integration is performed using the GPS quadrature in prolate spheroidal coordinates (see, e.g., Ref. [20]). Since the quadrature points differ from the original discretized coordinate values in the polar spherical coordinates for the wave packet $\Psi^L(\boldsymbol{r},t)$, we perform additional interpolation with the help of the GPS interpolation formula,

$$\Psi^L(r,\vartheta,t) = \sum_{i=i}^{N_x}\sum_{j=1}^{N_y}\Psi^L(r_i,\vartheta_j,t)\frac{P_{N_x+2}(x)-P_{N_x}(x)}{(x-x_i)P_{N_x+1}(x_i)(2N_x+3)} \times\frac{(2N_y+1)(1-y_j^2)P_{N_y}(y)}{(y-y_j)[P_{N_y-1}(y_j)-P_{N_y+1}(y_j)]}. \tag{34}$$

Here N_x and N_y are the numbers of discretized values for the radial r and angular ϑ coordinates, respectively. $P_{N_x}(x)$ and $P_{N_y}(y)$ are the Legendre polynomials; we use the Gauss-Lobatto discretization scheme for the radial coordinate and the Gauss-Legendre scheme for the angular coordinate. The relations between the variables x and y in the interval $[-1,1]$ and the coordinates are as follows:

TABLE I. Populations of the ground and the first two excited states of H after the 20 optical cycles laser pulse with the peak intensity 5×10^{13} W/cm^2. Calculations are based on Eq. (5) (A) and Eq. (18) (B). The number in parentheses indicates the power of 10.

State	Population after the pulse A	Population after the pulse B
$1s$	0.998561	0.998563
$2s$	0.699(−06)	0.694(−06)
$2p$	0.937(−06)	0.938(−06)

$$r = R_m \frac{1+x}{1-x+2R_m/R_b},$$

$$\cos\vartheta = y, \tag{35}$$

R_m and R_b being the mapping parameter and the end point for the radial coordinate, respectively. We used the GPS interpolation in our previous studies of above-threshold detachment of H^- and achieved a good accuracy [21]. Note that the interpolation of the wave packet does not depend on the final state and is performed before the electron energy and angular distributions are computed according to Eq. (28), thus reducing the computational effort. The total computation time of the ATI spectra depends on the length of the energy domain as well as on the desired resolution in the energy and angle domains. As our results show, for reasonable parameters, the time spent on the computation of the ATI spectra is of the same order as the time spent on solving TDSE for the wave packet (several hours using a modern Xeon-based workstation).

The calculations have been performed for relatively long (20 optical cycles) and short (4 optical cycles) laser pulses. The carrier frequency corresponds to the wavelength 800 nm, and the peak electric field strength F_0 used in Eq. (29) corresponds to the intensities of the continuous wave 5×10^{13}, 1×10^{14}, and 2×10^{14} W/cm^2. To test the accuracy of the method, we have calculated the populations of the ground and the first two excited states after the pulse using two different expressions for the transition amplitude, Eq. (5) (since the bound states are localized in space, it works even for the wave function with truncated large-distance domain) and Eq. (18). The results are presented in Table I. As one can see, the agreement is very good. Note that compared to simpler expression (5), calculations based on Eq. (18) involve two-center space integration and additional time integration. Another good accuracy test comes from comparison of the total ionization probability calculated from the energy and angle integration of the electron spectra [Eq. (28)] and that obtained from the normalization integral of the wave function after the pulse, Eq. (33). The results are summarized in Table II. As one can see, the agreement is quite good, within 1% for short pulses and about 2% for the longer pulse.

Figure 1 shows the high-resolution low-energy part of angle-integrated electron spectra for the 20 optical cycles laser pulse at the peak intensity 5×10^{13} W/cm^2. The results

TABLE II. Total ionization probability calculated from the norm of the wave function after the pulse, Eq. (33) (A) and by integration of the electron distributions, Eq. (28) (B), for different pulse durations, intensities, and CEP.

Intensity (W/cm^2)	Number of cycles	CEP (deg)	Total ionization probability A	Total ionization probability B
5×10^{13}	20	Any	0.00141	0.00144
1×10^{14}	4	0	0.00680	0.00675
1×10^{14}	4	45	0.00696	0.00699
1×10^{14}	4	90	0.00700	0.00706
1×10^{14}	4	135	0.00687	0.00688

do not show any noticeable dependence on CEP for this rather long pulse duration. The energy spectrum exhibits the well-known ATI structure with the peaks separated by a photon energy ω. To the right of each main peak, one can see several smaller subpeaks. In Ref. [22] appearance of subpeaks was attributed to the rapidly changing ponderomotive potential in the short laser pulse. Our comment is that this substructure is well understood for longer pulses and has an interference nature (see, e.g., Ref. [23]). Within the adiabatic approach [23], it is interpreted as a result of coherent summation of the two contributions which come from the leading and trailing edges of the pulse envelope. Interference maxima correspond to the particular points on the pulse envelope (or time moments). Since the intensity is different for these points, the ponderomotive and ac Stark shifts are also different and smaller than those at the top of the envelope. Hence the subpeaks are shifted to the right with respect to the main peak. The same explanation holds for short pulses as well, so far one can separate the carrier and the envelope.

The differential ionization probability [Eq. (20)] for the same laser pulse parameters is shown in Fig. 2 as a polar surface plot. The radial distance on the plot represents the energy, and the angle points to the direction where the electron is ejected. The color (density) corresponds to the values of the differential ionization probability; the color (density) scale is logarithmic. The rings on the plot represent the main

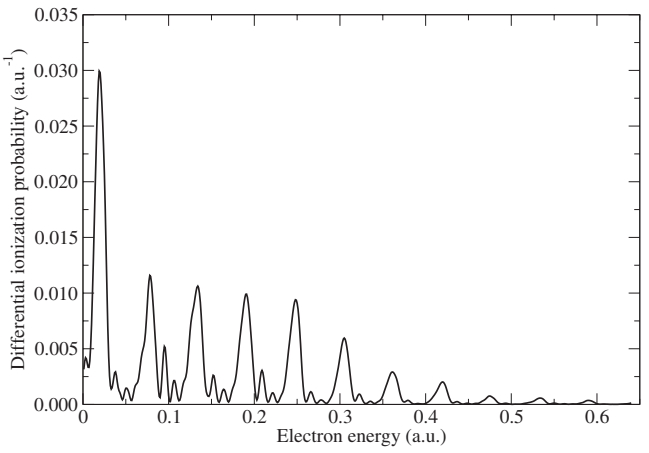

FIG. 1. Electron energy spectrum for the 20 optical cycle laser pulse with the peak intensity 5×10^{13} W/cm^2.

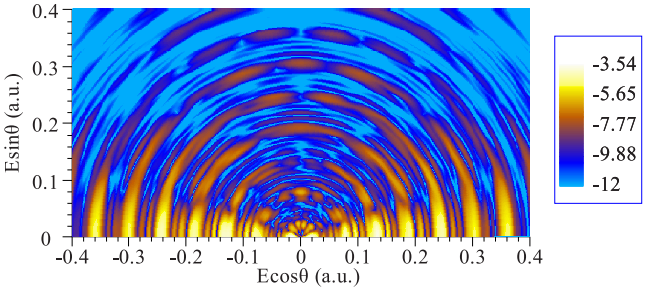

FIG. 2. (Color online) Energy-angle polar surface plot for the 20 optical cycle laser pulse with the peak intensity 5×10^{13} W/cm^2.

ATI peaks and their satellites. The inner ring corresponding to the first ATI peak exhibits radial stripe structure. The radial stripes have been discussed in the literature [9,24]; they are related to the nodal directions in the angular spectra. The number of the stripes is equal to the dominant value of the angular momentum in the final state plus one [24]. Figure 2 reveals six radial stripes and suggests that the dominant angular momentum for the specified laser-pulse parameters is equal to 5. As one can see from Fig. 2, the angular dependence of the differential probability shows almost perfect forward-backward symmetry. This is typical for long laser pulses; the symmetry is exact for the continuous wave [25]. The symmetry in the ionization probability can be observed also at the angle 90°. The rings corresponding to odd number of absorbed photons have nodes in this direction since the final state contains only odd angular momenta. The rings corresponding to even number of absorbed photons do not have nodes at 90°. Again, for the pulse of finite duration this symmetry holds only approximately; the longer the pulse, the more perfect symmetry can be observed.

For the laser pulses with 4 optical cycles, the calculations were carried out at the peak intensity 1×10^{14} W/cm^2. Short pulses manifest significant dependence of the differential and total ionization probability on CEP and broken forward-backward symmetry in the angular distributions. In Fig. 3, we present the high-resolution low-energy part of the angle-integrated differential ionization probability. As one can see, although the energy spectrum has ATI peaks, it does not exhibit equally spaced peak structure with the separation between the peaks equal to the carrier frequency, which is observed for the longer pulse (Fig. 1). This is because the pulse field contains the combination frequencies $\omega\pm\omega/N$. For $N=4$, these combination frequencies differ significantly from the carrier frequency. The energy spectrum can exhibit structures related to the carrier frequency as well as to the combination frequencies. The height and the position of the peaks in the spectrum depend on CEP. While the position of the most prominent peaks does not change much when CEP varies, their height changes significantly. In particular, the first and largest peak located just above the threshold is more than two times higher at $\alpha=\pi/2$ than at $\alpha=0$. CEP values correspond to the height of the first peak in the same order as they correspond to the total ionization probability (Table II). Note that for the second peak in the spectrum located approximately at 0.042 a.u., this order is reversed.

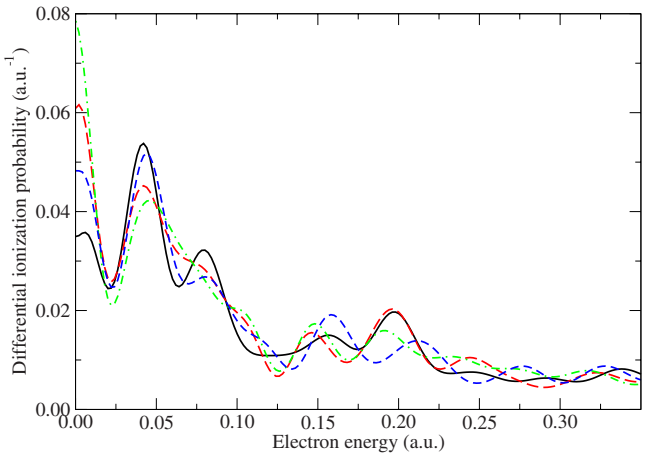

FIG. 3. (Color online) Electron energy spectrum for the 4 optical cycle laser pulse with the peak intensity 1×10^{14} W/cm^2. The carrier-envelope phase is 0 (solid black line), $\pi/4$ (long dash red line), $\pi/2$ (dot-dash green line), and $3\pi/4$ (short dash blue line).

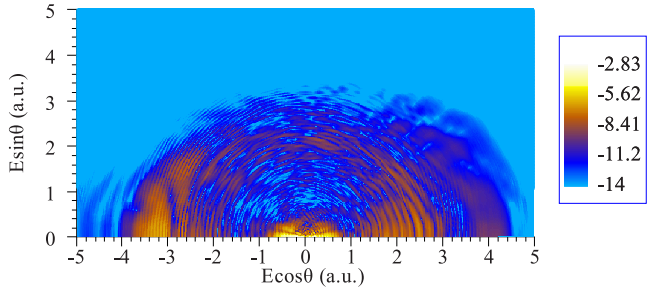

FIG. 4. (Color online) Energy-angle polar surface plot for the 4 optical cycle laser pulse with the peak intensity 1×10^{14} W/cm^2. The carrier-envelope phase is 0.

The polar surface plots of the differential ionization probability for 4 optical cycles pulses are presented in Figs. 4 and 5 for the CEP values 0 and $\pi/2$, respectively, and energy scale up to 5 a.u. The high-order ATI plateau is clearly seen in the energy interval between 1.5 and 3.5 a.u. where the probability distributions do not decrease with the increase in the energy, and noticeable fraction of electrons is ejected under large angles, which is a manifestation of the presence and importance of rescattering [7] for this region in the electron energy distributions.

In Fig. 6, we show the electron energy spectra from the high-order ATI of the atomic hydrogen at the peak intensity

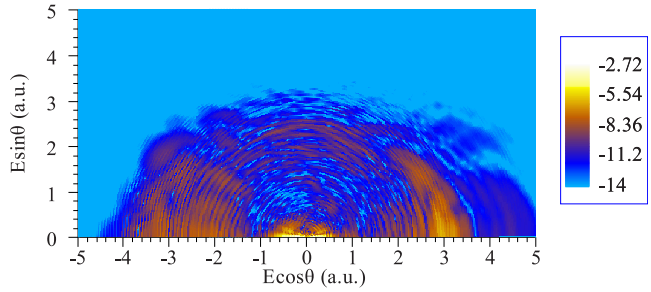

FIG. 5. (Color online) Energy-angle polar surface plot for the 4 optical cycle laser pulse with the peak intensity 1×10^{14} W/cm^2. The carrier-envelope phase is $\pi/2$.

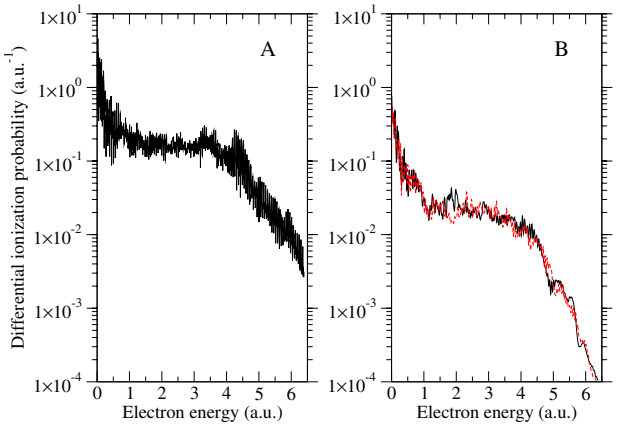

FIG. 6. (Color online) High-order ATI electron energy spectrum for the laser pulse with the peak intensity 2×10^{14} W/cm^2. The pulse duration is 20 optical cycles (panel A) and 4 optical cycles (panel B). In panel B, the CEP is 0 (solid black line) and $\pi/2$ (dashed red line).

2×10^{14} W/cm^2. At this intensity, the plateau part of the energy spectrum is long enough and well shaped. While the absolute values of the differential ionization probability are different for the pulse durations of 4 and 20 optical cycles, respectively, the cutoff positions in the spectra are the same. According to the semiclassical predictions [26], the cutoff is expected at the energy approximately equal to $10U_p$ [U_p is the ponderomotive potential; for linearly polarized laser fields, $U_p=F_0^2/(4\omega^2)$]. At the intensity 2×10^{14} W/cm^2, $10U_p\approx4.4$ a.u., and this value is in good agreement with our calculations, as one can see from Fig. 6.

Since the forward-backward symmetry does not hold for short laser pulses, the projection of the total momentum carried by the emitted electrons on the polarization direction of the field does not vanish and depends on CEP. In Fig. 7 we show the CEP dependence of the total momentum $\langle k_z\rangle$ and total energy $\langle E\rangle$ carried by the electrons. These quantities are defined as follows:

$$\langle k_z\rangle = \int_0^\infty dE \int d\Omega \sqrt{2E}\cos\vartheta \frac{\partial^2 P}{\partial E\,\partial\Omega}, \tag{36}$$

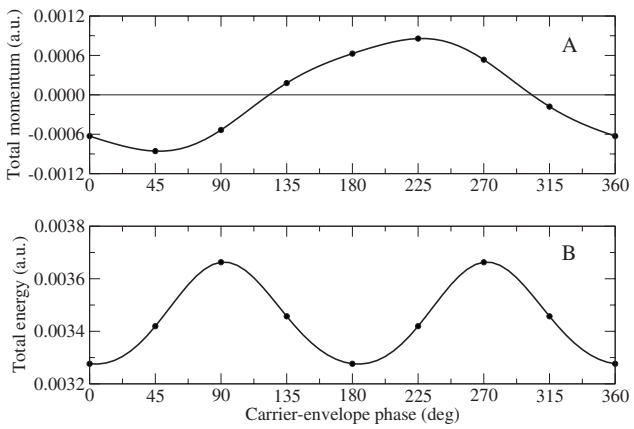

FIG. 7. CEP dependence of the total momentum (panel A) and total energy (panel B) carried by ejected electrons for the 4 optical cycle laser pulse with the peak intensity 1×10^{14} W/cm^2.

$$\langle E\rangle = \int_0^\infty dE \int d\Omega E \frac{\partial^2 P}{\partial E\,\partial\Omega}. \tag{37}$$

As one can see, the maximum energy is transferred to the electrons at CEP equal to $\pi/2$ and $3\pi/2$ (the same CEP values correspond to the largest total ionization probability, see Table II) while the maximum momentum is observed at $\alpha=\pi/4$ (in the backward direction) and at $\alpha=5\pi/4$ (in the forward direction). Since the laser pulse does not transfer any momentum to the electrons (zero-net-force condition), the recoil must be experienced by the atomic core. In principle, this phenomenon can be observed in the experiments and may help in CEP measurements.

IV. CONCLUSION

We have presented a method for calculations of electron distributions after above-threshold multiphoton ionization. The method makes use of the transition to the Kramers-Henneberger frame of reference where the interaction with the laser pulse is represented by an oscillating atomic core potential. Because the interaction potential is localized in space in the vicinity of the atomic core, only the core part of the time-dependent wave packet is required to calculate the ionization amplitudes and differential probabilities. As our study of ATI of the hydrogen atom shows, the method provides high accuracy in practical calculations including subtle effects related to the CEP dependence of the total ionization probability and the electron energy spectra. In particular, we predict a nonzero CEP-dependent total momentum gained by the electrons as a result of the interaction with the laser pulse.

For the hydrogen atom, we used the final-state wave functions which are available in the analytical form. Application of the method to analysis of ATI processes in many-electron atomic and molecular systems described with model potentials or within the framework of the self-interaction-free time-dependent density-functional theory (TDDFT) [27] will require construction of the proper final-state wave functions. The problem reduces to solution of the time-independent Schrödinger equation for continuum states with correct asymptotic behavior. Although the task is not simple, we expect the computational effort will be less than when solving the time-dependent Schrödinger equation. The work on the extension of the present approach to study of ATI processes of many-electron atomic and molecular systems using self-interaction-free TDDFT methods is currently in progress.

ACKNOWLEDGMENTS

This work was partially supported by the Chemical Sciences, Geosciences and Biosciences Division of the Office of Basic Energy Sciences, Office of Sciences, Department of Energy, by the National Science Foundation. We also would like to acknowledge the partial support of National Science Council of Taiwan (Grant No. 97-2112-M-002-003-MY3) and National Taiwan University (Grant No. 97R0066).

[1] T. Brabec and F. Krausz, Rev. Mod. Phys. **72**, 545 (2000).
[2] G. G. Paulus, F. Grasbon, H. Walther, P. Villoresi, M. Nisoli, S. Stagira, E. Priori, and S. De Silvestri, Nature (London) **414**, 182 (2001).
[3] A. Rudenko, K. Zrost, C. D. Schröter, V. L. B. de Jesus, B. Feuerstein, R. Moshammer, and J. Ullrich, J. Phys. B **37**, L407 (2004).
[4] C. M. Maharjan, A. S. Alnaser, I. Litvinyuk, P. Ranitovic, and C. L. Cocke, J. Phys. B **39**, 1955 (2006).
[5] M. Lewenstein, P. Balcou, M. Y. Ivanov, A. L'Huillier, and P. B. Corkum, Phys. Rev. A **49**, 2117 (1994).
[6] L. V. Keldysh, Zh. Eksp Teor. Fiz. **47**, 1945 (1964) [Sov. Phys. JETP **20**, 1307 (1965)]; F. H. M. Faisal, J. Phys. B **6**, L89 (1973); H. R. Reiss, Phys. Rev. A **22**, 1786 (1980).
[7] P. B. Corkum, Phys. Rev. Lett. **71**, 1994 (1993); J. L. Krause, K. J. Schafer, and K. C. Kulander, *ibid.* **68**, 3535 (1992).
[8] Z. Chen, T. Morishita, A. T. Le, and C. D. Lin, Phys. Rev. A **76**, 043402 (2007).
[9] D. G. Arbó, J. E. Miraglia, M. S. Gravielle, K. Schiessl, E. Persson, and J. Burgdörfer, Phys. Rev. A **77**, 013401 (2008).
[10] R. G. Newton, *Scattering Theory of Waves and Particles* (McGraw-Hill, New York, 1966).
[11] X. M. Tong, K. Hino, and N. Toshima, Phys. Rev. A **74**, 031405(R) (2006).
[12] A. Palacios, C. W. McCurdy, and T. N. Rescigno, Phys. Rev. A **76**, 043420 (2007).
[13] H. A. Kramers, *Collected Scientific Papers* (North Holland, Amsterdam, 1956).
[14] W. C. Henneberger, Phys. Rev. Lett. **21**, 838 (1968).
[15] D. B. Milošević, G. G. Paulus, D. Bauer, and W. Becker, J. Phys. B **39**, R203 (2006).
[16] M. Gavrila, J. Phys. B **35**, R147 (2002).
[17] F. H. M. Faisal, L. Dimou, H.-J. Stiemke, and M. Nurhuda, J. Nonlinear Opt. Phys. Mater. **4**, 701 (1995).
[18] *Handbook of Mathematical Functions*, edited by M. Abramowitz and I. Stegun (Dover, New York, 1965).
[19] D. A. Telnov and Shih-I Chu, J. Phys. B **37**, 1489 (2004).
[20] D. A. Telnov and Shih-I Chu, Phys. Rev. A **76**, 043412 (2007).
[21] D. A. Telnov and Shih-I Chu, Phys. Rev. A **50**, 4099 (1994).
[22] M. Wickenhauser, X. M. Tong, and C. D. Lin, Phys. Rev. A **73**, 011401(R) (2006).
[23] D. A. Telnov and S. I. Chu, J. Phys. B **28**, 2407 (1995).
[24] Z. Chen, T. Morishita, A. T. Le, M. Wickenhauser, X. M. Tong, and C. D. Lin, Phys. Rev. A **74**, 053405 (2006).
[25] V. N. Ostrovsky and D. A. Telnov, J. Phys. B **24**, L477 (1991).
[26] G. G. Paulus, W. Becker, W. Nicklich, and H. Walther, J. Phys. B **27**, L703 (1994); M. Lewenstein, K. C. Kulander, K. J. Schafer, and P. H. Bucksbaum, Phys. Rev. A **51**, 1495 (1995); J. Z. Kamiński, A. Jaroń, and F. Ehlotzky, *ibid.* **53**, 1756 (1996).
[27] S. I. Chu, J. Chem. Phys. **123**, 062207 (2005); J. J. Carrera, Shih-I Chu, and X. M. Tong, Phys. Rev. A **71**, 063813 (2005); J. Heslar, J. Carrera, D. Telnov, and S. I. Chu, Int. J. Quantum Chem. **107**, 3159 (2007).